UDK 544.022.6:676.017.62
Original scientific article/Izvirni znanstveni članek

ISSN 1580-2949
Mater. Tehnol.

OPTIMIZATION OF Al-BASED AMORPHOUS COATINGS BY WARM SPRAYING BASED ON A NUMERICAL SIMULATION AND A RESPONSE-SURFACE METHODOLOGY

OPTIMIZIRANJE AMORFNIH PREVLEK NA OSNOVI Al, IZDELANIH S TOPLIM NAPRŠEVANJEM; NUMERIČNA SIMULACIJA IN METODOLOGIJA ODGOVORA POVRŠINE

Deming Wang, Tingting Li, Nianchu Wu*
School of Mechanical Engineering, Liaoning Petrochemical University, Fushun 113001, PR China

Prejem rokopisa – received: 2024-07-17; sprejem za objavo – accepted for publication: 2024-10-24

doi:10.17222/mit.2024.1247

Al-based fully amorphous coatings with low porosity were prepared using a warm-spraying technology by combining numerical simulations and a response-surface methodology (RSM). The influences of spraying parameters (reactant flow rate, oxygen/fuel (O/F) ratio, coolant flow rate, and spraying distance) on the particle temperature and velocity were investigated using numerical simulation methods. On this basis, the response-surface equations for temperature and the velocity of the particles were established using the Box-Behnken Design (BBD) methods. The RSM was used to analyze the influence of the interactions between the spraying parameters on the temperature and the velocity of the particles. The optimum spraying parameters (OSP) predicted by the response optimizer were 0.012047 kg/s for the reactant flow rate, 0.011034 kg/s for the coolant flow rate, 2.7 for the O/F ratio, and 142 mm for the spraying distance. According to the OSP, the Al-based fully amorphous coatings with a porosity of 0.08% were obtained by warm-spraying experiments. This work provides guidance for the production of Al-based fully amorphous coatings with low porosity using warm spraying.

Keywords: Al-based amorphous coatings, warm spraying, numerical simulation, response-surface methodology

Popolne amorfne prevleke na osnovi Al z majhno poroznostjo so avtorji pripravili s tehnologijo toplega naprševanja. Optimizacijo postopka so izvedli s kombinacijo numeričnih simulacij in metodologije odgovora površine (RSM; angl.: response surface methodology). Ugotavljali so vpliv parametrov naprševanja (hitrosti pretoka reaktivnega plina, razmerje med kisikom in raaktivnim plinom (O/F; angl.: oxygen/fuel), hitrostjo pretoka ohlajevanlnega sredstva in razdaljo od šobe do mesta/površine naprševanja) na temperaturo delcev in njihovo temperaturo z uporabo metod numeričnih simulacij. Na tej osnovi so avtorji z uporabo BBD (angl,; Box-Behnken Desigen) metod postavili enačbe za odziv (odgovor) površine na temperaturo in hitrost delcev. RSM so uporabili za analizo vpliva interakcij med parametri naprševanja na temperaturo in hitrost delcev. Napovedali so optimalne parametre naprševanja (OSP; angl.: optimum spraying parameters) z optimizatorjem odziva in sicer: 0,012047 kg/s za pretok reaktivnega (zgorevalnega) plina, 0,011034 kg/s za pretok ohlajevalnega plina, za O/F razmerje 2,7 in za oddaljenost naprševanja 142 mm. V skladu z OSP so avtorji s praktičnimi preizkusi toplega naprševanja izdelali amorfne prevleke na osnovi Al s poroznostjo 0,08%. Ta raziskava po mnenju avtorjev predstavlja koristne napotke za izdelavo popolnih amorfnih prevlek na osnovi Al z nizko poroznostjo s postopkom toplega naprševanja.

Ključne besede: amorfne prevleke na osnovi Al, toplo naprševanje, numrična simulacija, metodologija odgovora površine

1 INTRODUCTION

Al-based amorphous coatings (AMCs) have broad application prospects in the fields of marine equipment, petrochemicals, and aerospace due to their excellent corrosion and wear resistance.[1–4] However, porosity and crystalline phase structures are inevitably generated in the preparation of Al-based AMCs.[5] The presence of porosity and crystalline phase structures reduces the corrosion and wear resistance of Al-based AMCs.[6] Therefore, it is necessary to find a suitable spraying process to prepare Al-based fully AMCs with low porosity.

Recently, the spraying processes used to produce Al-based AMCs include laser cladding,[7,8] cold spraying,[9–11] and thermal spraying.[12–18] Tan et al.[7] synthesized $Al_{85}Cu_{10}Zn_5$ AMCs by laser cladding under water-cooling conditions. However, there is sedimentation of nanocrystallines and intermetallic phases in the coatings due to the lower cooling rates. Jin et al.[11] prepared $Al_{86}Ni_8Co_1La_1Y_2Gd_2$ AMCs via cold spraying. Nevertheless, the Al-based amorphous alloy particles are easily crystallized during flight inside the cold spray gun. For thermal spraying, Cheng et al.[14] produced Al-Ni-Ti AMCs by arc spraying. Gao et al.[17] prepared $Al_{86}Ni_6Y_{4.5}Co_2La_{1.5}$ AMCs by high-velocity air-fuel spraying. Zhou et al.[18] sprayed $Al_{81}Ni_{10}Ti_9$ AMCs using plasma spraying. However, most of the Al-based amorphous alloy particles are completely molten or even over-molten in the thermal spraying process. As for warm spraying, it was developed based on the single-stage, high-velocity, oxygen-fuel (HVOF) thermal spray system.[19] The essence of the warm-spray system is to control the flame flow temperature by adding coolant of different mass flow rates to the mixing chamber.[20]

*Corresponding author's e-mail:
wunianchu@163.com (Nianchu Wu)

Based on the process characteristics mentioned above, the warm-spraying technique can maintain particle temperature in the range 850–1400 K and particle velocity in the range 620–1160 m/s.[20] Since the special construction of the warm-spray gun, the deposition temperature of particles is lower than that of other thermal spraying processes at the same particle velocity.[21] Therefore, warm spraying becomes a potentially ideal method to prepare the Al-based fully AMCs with low porosity.

To prepare Al-based fully AMCs with low porosity, there is a need to optimize the warm-spraying process to obtain the OSP. Thus, it is crucial to choose an appropriate optimization method. Presently, the methods used to optimize the spraying processes include design of experiments (DOE),[22–31] numerical simulation,[32–36] and machine learning (ML).[37–40] In the DOE methods, two-level factorial design,[23–25] the Taguchi method,[26–28] and RSM[29–31] are widely employed. Among them, the number of experiments for the two-level factorial design approach increases geometrically with the number of factors.[22] The Taguchi method is limited to single-response assemblies and is incapable of handling multi-response systems.[24] Compared with the two-level factorial design and the Taguchi method, the RSM has fewer experiments and can intuitively observe the effects of factor interactions on the response variable through 3D surfaces.[30] In the meantime, RSM can also obtain the OSP by analyzing the contours of the response surface.[31] For numerical simulation methods, due to revealing the complex reactions and fluid physics in the spraying process, numerical simulation methods were used to conduct many studies on the thermal spraying process.[32–36] Nevertheless, numerical simulation methods can only investigate single-factor variations and cannot consider the effects of multi-factor interactions on the response variables. As a result, the combination of numerical simulation and RSM becomes a novel approach for optimizing the spraying process to obtain OSP. Ren et al.[33] prepared WC–12Co coatings with low porosity using the HVOF spraying process based on combining numerical simulation and RSM. Chen et al.[35] predicted OSP by combining numerical simulation and RSM and prepared WC–12Co coatings with high corrosion and wear resistance using HVOF spraying experiments. However, the study for combining numerical simulation and RSM to predict OSP is rarely reported in terms of the warm-spraying process. Li et al.[36] only studied the sensitivity of the warm-spraying process parameters to particle-deposition temperature and velocity based on numerical simulation and RSM. Therefore, the combination of numerical simulation and RSM has research value for optimizing the parameters of the warm-spraying process. As for ML approaches, it is the scientific investigation of algorithms and statistical models used by computer systems to carry out particular missions.[38] However, the applicability and accuracy of the ML approaches are strongly affected by he data size and it is tedious work to obtain enough in - formation about the data. In summary, it is important to prepare Al-based fully AMCs with low porosity using warm-spraying technology by combining numerical simulation and RSM.

In this study, the process parameters for the production of Al-based AMCs by warm spraying were optimized by combining numerical simulation and RSM. The influences of the spraying parameters (reactant flow rate, O/F ratio, coolant flow rate, and spraying distance) on the particle temperature and velocity were investigated using numerical simulation methods. Moreover, the RSM was used to analyze the influence of the interactions between the spraying parameters on the particle temperature and velocity and to predict the OSP. According to the OSP, the Al-based fully AMCs with low porosity were prepared using warm-spraying experiments.

2 MATHEMATICAL MODELLING AND EXPERIMENTAL METHODS

2.1 Mathematical modelling

Figure 1 depicts the structure and dimensions of the warm-spray system. A is the propylene and oxygen inlet, B is the coolant inlet, and C is the carrier gas and particle inlet. The computational areas of the numerical simulation include the combustion chamber (I), convergent nozzle (II), mixing chamber (III), converging-diverging (C-D) nozzle (IV), barrel (V), and free jet region (VI).

Figure 2 illustrates the computational grids and boundary conditions for the warm-spray gun model. Since the warm-spray gun is an axisymmetric structure, only half of the two-dimensional computational region is modeled. During the modeling process, the whole computational area is meshed using the quadrilateral structural cell. There are 93,160 cells, 187,780 faces, and 94,621 nodes in the entire computational domain. The

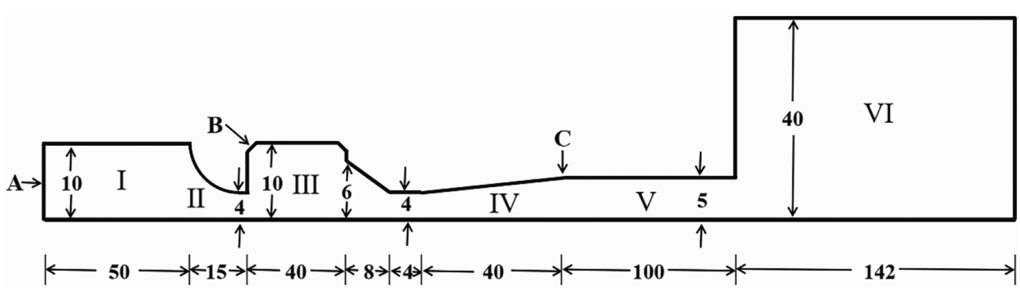

Figure 1: Schematic of structure and dimensions for the warm-spray system

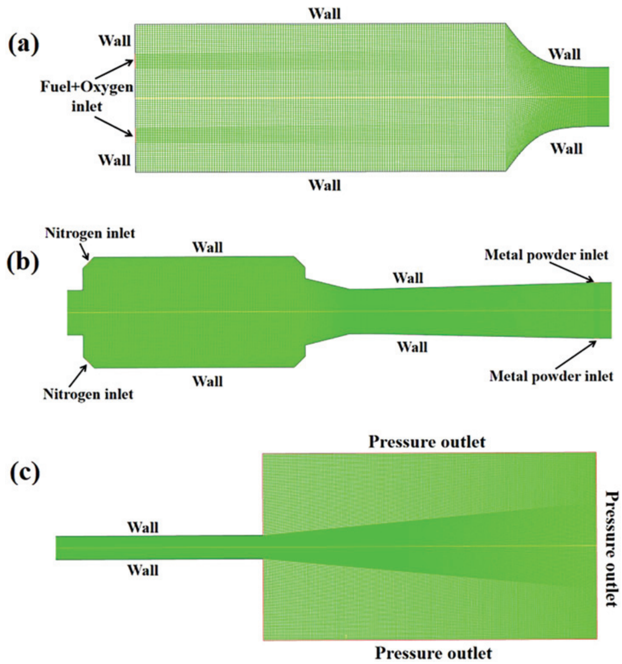

Figure 2: Computational grids and boundary conditions for: a) combustion chamber and convergent nozzle, b) mixing chamber and C-D nozzle, c) barrel and free jet region

grids of the fuel-oxygen inlet, C-D nozzle, and free jet regions are encrypted to precisely depict the flame flow characteristics and particle in-flight behaviors. The defined types of boundary conditions are mass flow inlet, axis, wall, and pressure outlet. The mass flow rates of the A, B, and C inlets are respectively 0.012047 kg/s, 0.011034 kg/s, and 0.00054 kg/s. The temperatures of the three mass flow inlets are all 300 K. The pressure value in the free jet region is assumed to be 1 atm. It is usually supposed that the wall is non-slip and the temperature is 350 K. The material characteristics of the $Al_{86}Ni_{6.75}Co_{2.25}Y_{3.25}La_{1.75}$ amorphous alloy powders used in this paper are as follows:[2] T_S = 899 K, T_L = 1200 K, ρ_p = 3300 kg/m^3, and c_p = 834.03 J/(kg·K).

2.2 Model description

The conservation equations of mass, momentum, and energy constitute the compressible reactive Navier-Stokes equations for the gas-phase model. The control equations in the Cartesian coordinate system are given below:[32]

Mass conservation:

$$\frac{\partial \rho}{\partial t}+\frac{\partial(\rho u_i)}{\partial x_i}=0 \tag{1}$$

Momentum conservation:

$$\begin{aligned}&\frac{\partial}{\partial t}(\rho u_i)+\frac{\partial}{\partial x_j}(\rho u_i u_j)=\\&=-\frac{\partial p}{\partial x_i}+\frac{\partial}{\partial x_j}(\tau_{ij})_{\mathrm{eff}}+\frac{\partial}{\partial x_j}\left(-\overline{\rho u_i' u_j'}\right)\end{aligned} \tag{2}$$

Energy conservation:

$$\begin{aligned}&\frac{\partial}{\partial t}(\rho E)+\frac{\partial}{\partial x_i}\left[u_i(\rho E+p)\right]=\\&=\frac{\partial}{\partial x_j}\left(k_{eff}\frac{\partial T}{\partial x_j}+u_i(\tau_{ij})_{\mathrm{eff}}\right)+S_{\mathrm{h}}\end{aligned} \tag{3}$$

where T is the temperature, ρ is the density, p is the pressure, k_{eff} is the effective thermal conductivity, t is the turbulent environment, u is the velocity, x is the coordinate, τ_{ij} is the deviatoric stress tensor, E is the enthalpy, S_h is reaction source energy, and $(\tau_{ij})_{eff}$ is the sum of effective values for the viscosity turbulence and non-turbulence.

Compared to other k-ε models, the renormalization group (RNG) k-ε model has a powerful ability to simulate complex shear flows. The RNG k-ε model and the non-equilibrium wall functions are employed to predict the flow characteristics of the turbulent center in the warm-spray system. The model expressions are shown below:[33]

Turbulent kinetic energy:

$$\frac{\partial}{\partial x_j}(\rho k u_j)=\frac{\partial}{\partial x_j}\left(\alpha_{\mathrm{k}}(\mu+\mu_{\mathrm{t}})\frac{\partial k}{\partial x_j}\right)+P_{\mathrm{k}}-\rho\varepsilon-Y_{\mathrm{M}} \tag{4}$$

Rate of turbulent kinetic energy dissipation:

$$\begin{aligned}&\frac{\partial}{\partial x_j}(\rho\varepsilon u_j)=\\&=\frac{\partial}{\partial x_j}\left(\alpha_\varepsilon(\mu+\mu_{\mathrm{t}})\frac{\partial\varepsilon}{\partial x_j}\right)+\frac{\varepsilon}{k}(c_1P_{\mathrm{k}}-\rho\varepsilon c_2)-R_\varepsilon\end{aligned} \tag{5}$$

$$P_{\mathrm{k}}=\mu_{\mathrm{t}}\left(\frac{\partial u_i}{\partial x_j}+\frac{\partial u_j}{\partial x_i}\right)\frac{\partial u_i}{\partial x_j}-\frac{2}{3}\left(\rho k+\mu_{\mathrm{t}}\frac{\partial u_l}{\partial x_l}\right)\frac{\partial u_k}{\partial x_k} \tag{6}$$

where k is the turbulent kinetic energy, μ is the molecular viscosity, α is the inverse effective Prandtl number, P_k is the turbulent kinetic energy production rate, μ_t is the turbulent viscosity, ε is the turbulence dissipation rate, and R_ε is an additional term for the ε equation; c_1 = 1.42 and c_2 = 1.68.

The reaction process inside the combustion chamber was simulated using the eddy-dissipation model (EDM)[32] in the warm-spray system. The model hypothesizes that the combustion reaction rate is affected by the turbulent mixing motions of propylene and oxygen, and not determined by the chemical reaction rate.

$$R_{\mathrm{F}}=\frac{\rho\varepsilon}{k}A\min\left[m_{\mathrm{F}},\frac{m_0}{S_0},B\frac{m_{\mathrm{P}}}{S_{\mathrm{P}}}\right] \tag{7}$$

where

$$S_0\equiv\frac{n_0M_0}{n_{\mathrm{F}}M_{\mathrm{F}}} \tag{8}$$

$$S_{\mathrm{P}} \equiv \frac{n_{\mathrm{P}} M_{\mathrm{P}}}{n_{\mathrm{F}} M_{\mathrm{F}}} \tag{9}$$

A and B are empirical constants; A = 4 and B = 0.5.

The burning of hydrocarbons is an unknown and complex process. The combustion process involves numerous elementary reactions and strong thermal atomic vibrations, which lead to the main reactants decomposing into many low molecular weight species, including CO, O, H, H_2, H_2O, CO_2, OH, and O_2. The chemical equilibrium equation is described as:[36]

$$C_3H_6 + 4.307O_2 \rightarrow 2.004H_2O + 1.903CO + 0.432H_2 + 0.692O_2 + 0.382H + 0.745OH + 1.097CO_2 + 0.388O \tag{10}$$

The discrete phase model (DPM)[34] can consider both one-way and two-way coupling between the gas and the particle phases. The model uses the gas-phase momentum and heat-transfer equations to solve the temperature and velocity of the particles based on the Euler-Lagrange method. Compared with the gas flow field, the volume flow of particles is less than 12 %,[41] so the effect of particles on the gas phase can be ignored. Thus, this study uses the one-way coupling approach to simulate the interaction between the gas and the particle phases. When other external forces are ignored, the particles are mainly affected by drag forces during flight. The following motion equations for spherical particles are given in:[32]

$$m_{\mathrm{p}} \frac{\mathrm{d}U_{\mathrm{p}}}{\mathrm{d}t} = \frac{1}{2} \rho_{\mathrm{g}} A_{\mathrm{p}} C_{\mathrm{D}} (U_{\mathrm{g}} - U_{\mathrm{p}}) \left| U_{\mathrm{g}} - U_{\mathrm{p}} \right| + F_x \tag{11}$$

where m_{p} is the particle mass, U_{p} is the particle velocity, ρ_g is the gas density, A_{p} is the surface area of the particle, C_D is the drag coefficient, U_g is the gas velocity, and F_x is the particle force source term.

The thermal equilibrium equation of particles is described as:[34]

$$m_{\mathrm{p}} C_{\mathrm{p}} \frac{\mathrm{d}T_{\mathrm{p}}}{\mathrm{d}t} = A_{\mathrm{p}} h_{\mathrm{c}} (T_{\mathrm{g}} - T_{\mathrm{p}}) \tag{12}$$

where T_g is the gas temperature, T_{p} is the particle temperature, C_{p} is the particle specific heat, and h_{c} is the heat-transfer coefficient.

2.3 Experimental method

The coating materials used in the study were $Al_{86}Ni_{6.75}Co_{2.25}Y_{3.25}La_{1.75}$ amorphous alloy with the best glass-forming ability.[2] The powders were produced by the gas-aerosolization method in a high-purity nitrogen environment. The powders with sizes of 10–50 µm were sieved using the conventional sieve-analysis methods for the production of Al-based AMCs. The sprayed substrate used was AA 2024 plates with dimensions of 100 mm × 30 mm × 2 mm. Before conducting the spraying experiment, the substrate is sanded, degreased, dried, and sandblasted, which helps the deposition of the spray particles. The operating parameters for the warm-spraying experiment are as follows: 22.1 m^3/h for the oxygen flow rate, 22.8 L/h for the propylene flow rate, 31.8 m^3/h for the cooling flow rate, 30 g/min for the particle feeding rate, and 142 mm for the spraying distance.

The microstructures of the powders and coatings were characterized using scanning electron microscopy (SEM, Quanta 600). An X-ray diffractometer (XRD, Tokyo, Japan) was utilized to determine the phase structure constituents of powders and coatings under monochromated Cu-K_α radiation. Image Pro Plus 6.0 software was used to analyze the SEM micrographs of the Al-based AMCs and evaluate their porosity.

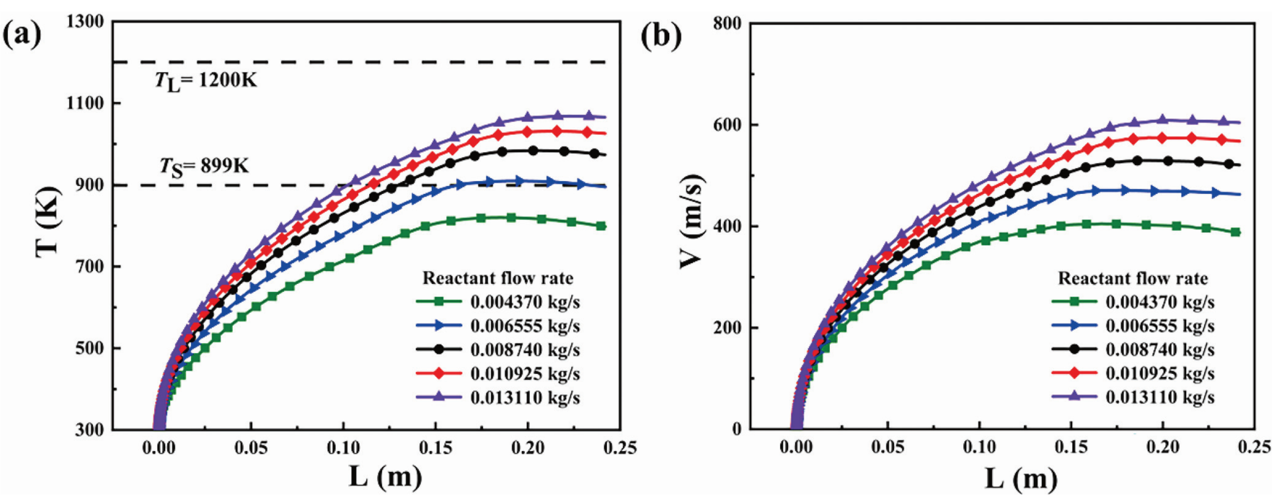

Figure 3: Effects of reactant flow rate on the particle: a) temperature and b) velocity

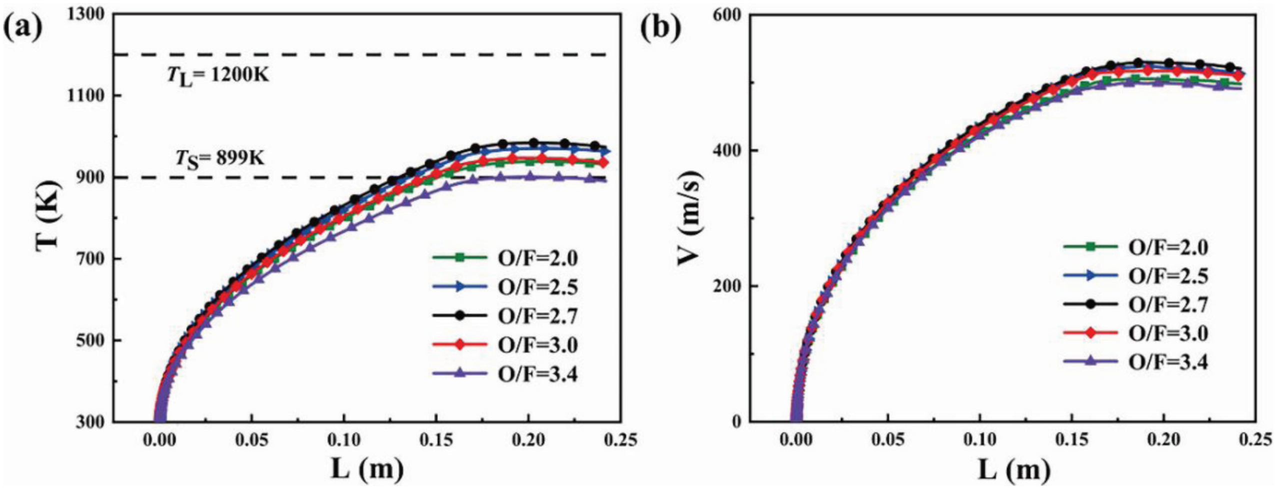

Figure 4: Effects of the O/F ratio on the particle: a) temperature and b) velocity

3 RESULTS AND DISCUSSION

3.1 Numerical simulation

3.1.1 Effects of the reactant flow rate on particle in-flight behaviors

Figure 3 shows the temperature and velocity of a 30 µm particle for different reactant flow rates (0.004370–0.013110 kg/s). The particle temperature rises with increasing reactant flow rate (**Figure 3a**). At a low reactant flow rate (0.004370 kg/s), the 30-µm particles always remain in a solid state during flight. With an increasing reactant flow rate, the particle temperature gradually rises. When the reactant flow rate is between 0.006555 and 0.013110 kg/s, the 30 µm particles hit the substrate in a semi-molten state because their temperature is between T_S and T_L. There is a similar influence of the reactant flow rate on particle velocity as there is on particle temperature (**Figure 3b**). The particle velocity rises as the reactant flow rate increases as well. When the reactant flow rate is increased from 0.004370 kg/s to 0.013110 kg/s, the velocity of the 30 µm particles when they impact the substrate increases from 387.57 m/s to 604.39 m/s. This is due to the favorable environment for particle acceleration provided by the gas flow field corresponding to the reactant flow rate.

3.1.2 Effects of the O/F ratio on particle in-flight behaviors

Figure 4 shows the temperature and velocity of a 30 µm particle for different O/F ratios (2.0–3.4). The 30 µm particle has the highest temperature at an O/F ratio of 2.7 (**Figure 4a**). The 30 µm particles can reach a semi-molten state before impacting the substrate when the O/F ratio is between 2.0 and 3.4. As the O/F ratio rises from 2.0 to 3.4, the particle temperature first increases (2.0–2.7) and then decreases (2.7–3.4). The O/F ratio has a smaller effect on particle velocity compared with the particle temperature (**Figure 4b**). The 30 µm particle has the highest velocity at an O/F ratio of 2.7. Inside the barrel, the influence of the O/F ratio on particle velocity can be ignored. Outside the barrel, the particle velocity also first rises (2.0–2.7) and then drops (2.7–3.4) as the O/F ratio increases (2.0–3.4).

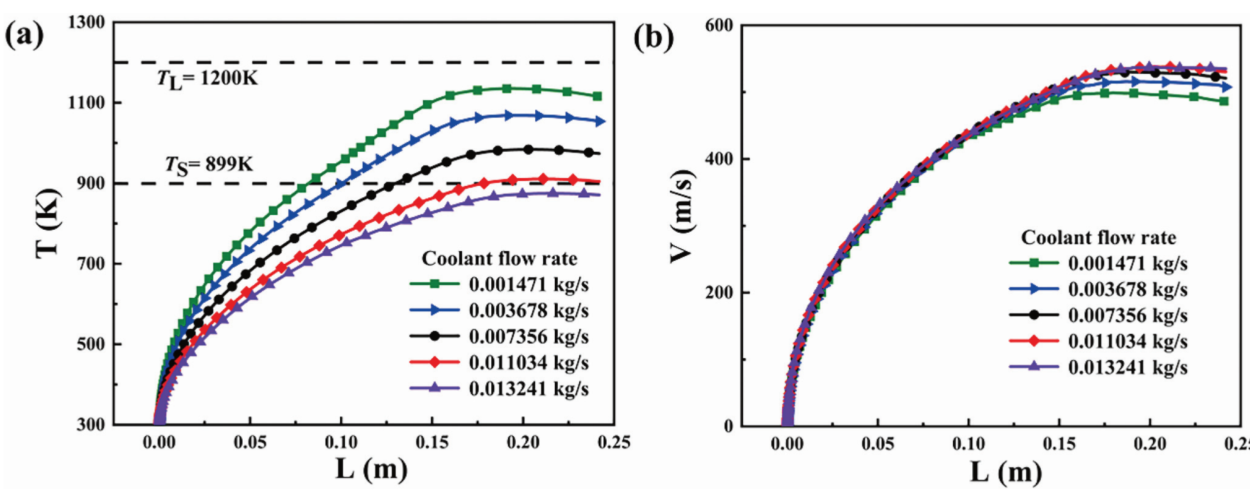

Figure 5: Effect of coolant flow rate on the particle: a) temperature and b) velocity

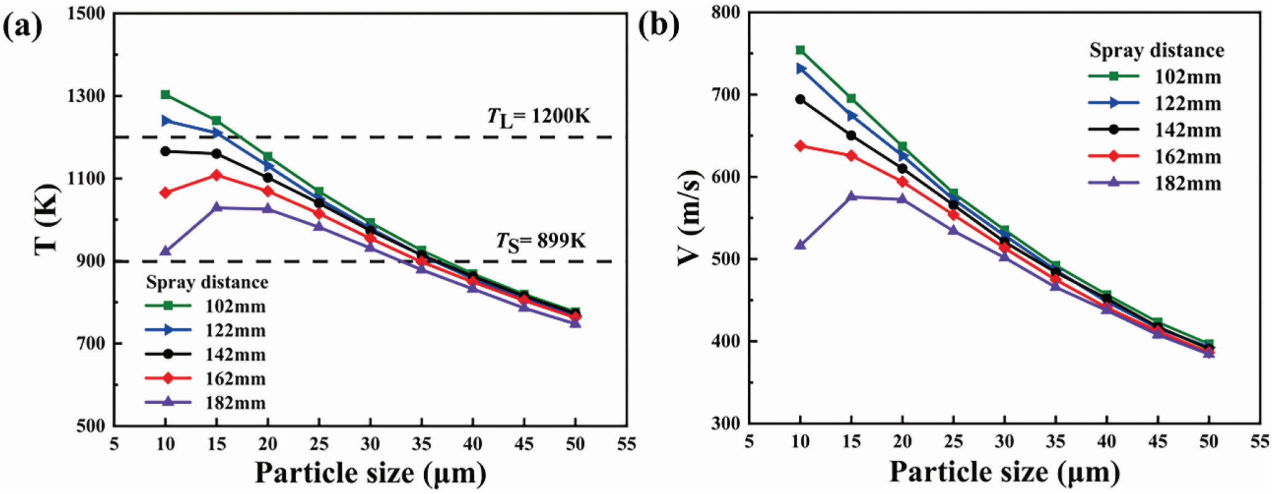

Figure 6: Effect of spraying distance on: a) axial temperature and b) axial velocity of particles when they impact the substrate

3.1.3 Effects of the coolant flow rate on particle in-flight behaviors

Figure 5 shows the temperature and velocity of a 30 μm particle for different coolant flow rates (0.001471–0.013241 kg/s). The particle temperature drops with increasing coolant flow rates (**Figure 5a**). When the coolant flow rate is between 0.001471 and 0.011034 kg/s, the 30 μm particles hit the substrate in a semi-molten state. At higher coolant flow rates (0.013241 kg/s), the 30 μm particles always remain in a solid state during flight. The coolant flow rate has the opposite influence on particle velocity as it does on particle temperature (**Figure 5b**). The particle velocity is positively correlated with the coolant flow rate and this effect is noticeable outside the barrel.

3.1.4 Effects of the spraying distance on particle in-flight behaviors

Figure 6 shows the axial temperature and axial velocity of the particles when they impact the substrate for 10–50 μm particles. Compared with the large-size particles, the axial temperature and velocity of the small-size particles (less than 25 μm) are more easily affected by the spraying distance. The axial temperature of the particles drops as the spraying distance lengthens (**Figure 6a**). The particle axial temperature falls with increasing particle size when the spraying distance is fixed. When the spraying distance is short (less than 122 mm), the 10 μm and 15 μm particles can completely melt before impacting the substrate. The 10–35 μm particles hit the substrate in a semi-molten state at a spraying distance of 142 mm. When the spraying distance is more than 162 mm, particles larger than 35 μm remain in a solid state when they impact the substrate. Due to the limited glass-forming ability of Al-based amorphous alloys, particles of small to medium size are more easily able to form Al-based fully AMCs.[2] The axial velocity of the particles decreases as the spraying distance increases (**Figure 6b**). The small-size particles have higher axial velocities than the large-size particles when the spraying distance is fixed. In summary, the 10–35 μm particles hit the substrate at a high velocity and in a semi-molten state for a spraying distance of 142 mm.

3.2 Optimization and analysis of RSM

3.2.1 Modeling of response surface equations and reasonability analysis

In this study, the RSM was used to optimize the process of preparing Al-based AMCs by warm spraying and predict the OSP. The RSM is an approach to expressing relationships between nonlinear functions by using complex multinomials.[36] The method expresses the nonlinear effects of the various factor interactions on the response variable by using images to predict the OSP. The second-order polynomial equation is as follows:[29]

$$Y=\beta_0+\sum_{i=1}^{k}\beta_i x_i+\sum_{i=1}^{k}\beta_{ii}x_i+\sum_{1\le i\le j}^{k}\beta_{ij}x_i x_j+\varepsilon \quad (13)$$

where k is the number of design factors, x is the design factor, Y is the response variable, β_0 is the response average, and ε is the error; β_i, β_{ii}, and β_{ij} represent the linear, quadratic, and interaction coefficients, respectively.

The RSM is constructing and optimizing multi-response surfaces simultaneously based on the desirability function method.[36] Due to the different optimization goals, the conversion formulas of the response function also differ. The minimum, target, and maximum of the response function are shown in Equations (14)–(16)[33], respectively. To obtain optimization solutions for different response functions, the overall desirability is calculated by the geometric average, as shown in Equation (17).[33]

$$d_r^{\min} = \begin{cases} 0, & f_r(X) > B \\ \left(\dfrac{f_r(X) - B}{A - B} \right)^s, & A \le f_r(X) \le B \\ 1, & f_r(X) > A \end{cases} \quad (14)$$

$$d_r^{\text{target}} = \begin{cases} \left(\dfrac{f_r(X) - A}{t_0 - A} \right)^{s_1}, & \mathrm{A} \le f_r(X) \le t_0 \\ \left(\dfrac{f_r(X) - B}{t_0 - B} \right)^{s_2}, & t_0 \le f_r(X) \le B \\ 0, & \text{otherwise} \end{cases} \quad (15)$$

$$d_r^{\max} = \begin{cases} 0, & f_r(X) < A \\ \left(\dfrac{f_r(X) - A}{B - A} \right)^s, & A \le f_r(X) \le B \\ 1, & f_r(X) > B \end{cases} \quad (16)$$

$$D = \left(\prod_{r=1}^{R} d_r \right)^{1/R} \quad (17)$$

where A is the minimum value, t_0 is the target value, B is the maximum value, and $f_r(X)$ is the response equation fitted by RSM.

Table 1: Design factor coding and level

Factor	Variable	Level		
		–1	0	+1
Reactant flow rate (kg/s)	*F*	0.004370	0.008740	0.013110
O/F ratio	*R*	2.0	2.7	3.4
Coolant flow rate (kg/s)	*C*	0.003678	0.007356	0.011034
Spraying distance (mm)	*L*	102	142	182

The RSM includes the Central Composite Design (CCD) method and the BBD method.[36] The CCD method is usually applied to experiments with multi-factor and multi-level. The BBD method is usually applied to trials with few factors and levels (below 5 factors and 3 levels). In this paper, the design factors include reactant flow rate (*F*), O/F ratio (*R*), coolant flow rate (*C*), and spraying distance (*L*). The deposition temperature (*Pt*) and deposition velocity (*Pv*) of the particles are selected as the response variables. Therefore, this study applies the BBD method to devise the random test scheme. The codes and levels of the design factors are presented in **Table 1**. The random test scheme and response results are summarised in **Table 2**.

Based on the summative analysis of the stochastic test program and response results (**Table 2**), the relationships between design factors and response values were

Table 2: RSM random scheme and results

Order number	*F* (kg/s)	*R*	*C* (kg/s)	*L* (mm)	*Pt* (K)	*Pv* (m/s)
1	0.004370	3.4	0.007356	142	732.88	365.16
2	0.008740	2.7	0.007356	142	953.85	518.62
3	0.013110	2.7	0.011034	142	996.59	608.56
4	0.013110	2.7	0.007356	182	1045.63	596.64
5	0.008740	2.7	0.011034	102	910.88	537.59
6	0.004370	2.7	0.003678	142	900.99	345.36
7	0.008740	2.7	0.003678	102	1067.08	513.97
8	0.013110	3.4	0.007356	142	979.38	579.21
9	0.008740	2.7	0.003678	182	1018.35	489.34
10	0.004370	2.7	0.011034	142	737.24	396.12
11	0.004370	2.0	0.007356	142	777.64	368.40
12	0.008740	3.4	0.011034	142	831.13	501.66
13	0.013110	2.7	0.003678	142	1143.20	593.15
14	0.008740	2.0	0.007356	182	909.86	480.11
15	0.004370	2.7	0.007356	182	750.55	349.27
16	0.013110	2.7	0.007356	102	1063.88	608.90
17	0.008740	2.0	0.007356	102	939.12	506.63
18	0.008740	3.4	0.003678	142	962.16	472.06
19	0.008740	2.7	0.007356	142	953.85	518.62
20	0.008740	3.4	0.007356	102	900.72	504.52
21	0.008740	2.7	0.011034	182	884.08	514.44
22	0.008740	2.0	0.003678	142	1005.31	472.44
23	0.013110	2.0	0.007356	142	1018.61	582.27
24	0.008740	2.7	0.007356	142	953.85	518.62
25	0.008740	3.4	0.007356	182	864.20	480.82
26	0.008740	2.0	0.011034	142	873.01	510.68
27	0.004370	2.7	0.007356	102	816.09	400.25

Table 3: Analysis of variance test results for particle-deposition temperature

Source	Freedom	Seq SS	Distribution	Adj SS	Adj MS	*F* value	*P* value
Model	8	291230	99.61 %	291230	36404	575.64	<0.0001
Linear	4	267351	91.44 %	267351	66838	1056.87	<0.0001
F	1	195560	66.89 %	195560	195560	3092.30	<0.0001
R	1	5337	1.83 %	5337	5337	84.40	<0.0001
C	1	62231	21.29 %	62231	62231	984.03	<0.0001
L	1	4223	1.44 %	4223	4223	66.77	<0.0001
Square	3	23320	7.98 %	23320	7773	122.92	<0.0001
F×*F*	1	3112	1.06 %	4615	4615	72.97	<0.0001
R×*R*	1	18224	6.23 %	14298	14298	226.08	<0.0001
C×*C*	1	1984	0.68 %	1984	1984	31.37	<0.0001
Interaction	1	559	0.19 %	559	559	8.84	0.008
F×*L*	1	559	0.19 %	559	559	8.84	0.008
Error	18	1138	0.39 %	1138	63		
Lack of fit	16	1138	0.39 %	1138	71		
Pure error	2	0	0.00 %	0	0		
Total	26	292368	100.00 %				

R-Squared = 99.61 %, Adj R-Squared = 99.44 %, Pred R-Squared = 98.82 %.

Table 4: Analysis of variance test results for particle deposition velocity

Source	Freedom	Seq SS	Distribution	Adj SS	Adj MS	*F* value	*P* value
Model	9	161591	99.74 %	161591	17955	736.71	<0.0001
Linear	4	155539	96.01 %	155539	38885	1595.52	<0.0001
F	1	144752	89.19 %	144752	144752	6178.03	<0.0001
R	1	2783	1.72 %	2783	2783	114.17	<0.0001
C	1	5837	3.76 %	5837	5837	381.59	<0.0001
L	1	2167	1.34 %	2167	2167	88.90	<0.0001
Square	3	5364	3.31 %	5364	1788	73.37	<0.0001
F×*F*	1	2640	1.63 %	3791	3791	155.55	<0.0001
R×*R*	1	2581	1.59 %	2723	2723	111.72	<0.0001
C×*C*	1	143	0.09 %	143	143	5.85	0.027
Interaction	2	687	0.42 %	687	344	14.10	<0.0001
to*F*×*C*	1	312	0.19 %	312	312	12.82	0.002
F×*L*	1	375	0.23 %	375	375	15.38	0.001
Error	17	414	0.26 %	414	24		
Lack of fit	15	414	0.26 %	414	28		
Pure error	2	0	0.00 %	0	0		
Total	26	162005	100.00 %				

R-Squared = 99.74 %, Adj R-Squared = 99.61 %, Pred R-Squared = 99.25 %.

expressed by using multiple-regression equations. The response-surface equations for particle temperature (Pt) and particle velocity (Pv) were eventually derived as shown below:

$$Pt = 307.6 + 44993F + 507.8R - 39356C - 1.06L - 1452214F \times F - 99.62R \times R + 1344260C \times C + 67.6F \times L \quad (18)$$

$$Pv = -88.3 + 44822F + 232.7R + 14249C - 0.820L - 1316248F \times F - 43.47R \times R - 360465C \times C - 549840F \times C + 55.4F \times L \quad (19)$$

where F is the reactant flow rate, R is the O/F ratio, C is the coolant flow rate, and L is the spraying distance; Pt and Pv represent the response surface equations for particle temperature and particle velocity, respectively.

The analysis of the variance test results for particle-deposition temperature is shown in **Table 3**. The F value indicates the effect level of the design factor on the response variable. The larger the F value, the higher the effect level. The P value indicates the significant level of the design factor. The design factor is significant when $P < 0.05$ and more significant when $P < 0.001$. For the F value, the effect level of the design factor on particle-deposition temperature is L (66.77) < R (84.40) < C (984.03) < F (3092.30). For the P value, the linear terms (F, R, C, and L), square terms (F×F, R×R, and C×C), and interaction terms (F×L) all have a conspicuous effect on Pt. R-Squared is 99.61 %, which shows that the response surface model of particle-deposition temperature has a relatively accurate predictive precision. The margin between Adj R-Squared (99.44%) and

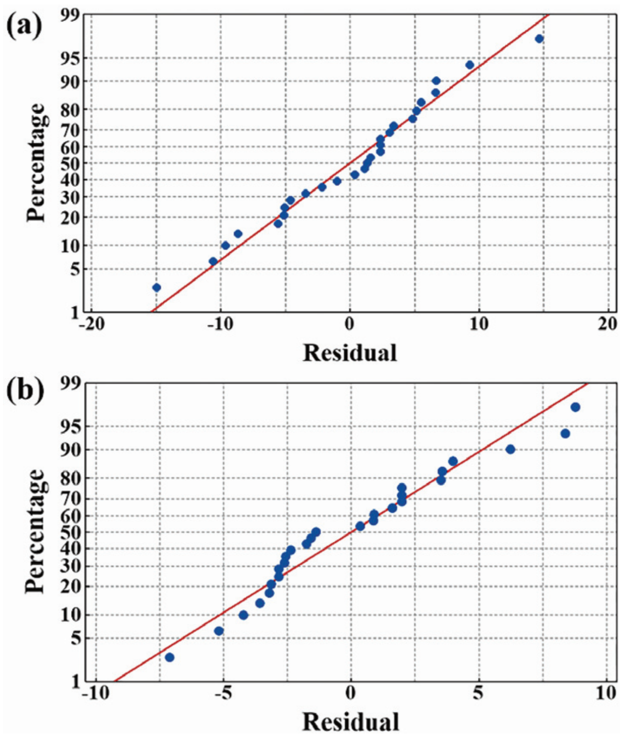

Figure 7: Graphs of the residual normal distributions for: a) particle-deposition temperature and b) particle deposition velocity

Pred R-Squared (98.82 %) is below 0.1, showing that the response-surface model of particle-deposition temperature has stronger predictive ability.

The analysis of the variance test results for particle-deposition velocity is shown in **Table 4**. For the *F* value, the effect level of the design factor on particle deposition velocity is *L* (88.90) < *R* (114.17) < *C* (381.59) < *F* (6178.03). For the *P* value, the linear terms (*F*, *R*, *C*, and *L*), square terms (*F*×*F*, *R*×*R*, and *C*×*C*), and interaction terms (*F*×*C* and *F*×*L*) all have a prominent effect on *Pv*. R-Squared is 99.74 %, which shows that the response surface model of particle deposition velocity has a relatively accurate predictive precision. The margin between Adj R-Squared (99.61 %) and Pred R-Squared (99.25 %) is below 0.1, showing that the response surface model of particle deposition velocity has stronger predictive ability. In summary, the response surface models for both temperature and velocity of particle deposition have higher predictive precision.

Figure 7 illustrates the probability plots of the residual normal distributions for particle-deposition temperature and velocity. In **Figure 7a**, the residual data points of particle-deposition temperatures are approximately linearly distributed and fluctuate within a permissible range, indicating that the residuals are normally distributed. In **Figure 7b**, the residual data of particle deposition velocity are essentially dispersed around a straight line, indicating that the normal distribution of the residual terms is acceptable. The residual plots further demonstrate the validity of the response surface model for temperature and velocity of particle deposition, which is in agreement with the variance analysis results.

3.2.2 The analysis of RSM results

Figure 8 presents the effects of factor interactions on particle temperature. The influence of the interaction between *F* and *R* on *Pt* is displayed in **Figure 8a**. When *F* and *R* increase at the same time, *Pt* first rises and then falls slightly. *Pt* is always the maximum value when *F* is fixed and *R* is 2.7. **Figure 8b** illustrates the influence of the interaction between *F* and *C* on *Pt*. The effect of *F* on *Pt* is opposite to the effect of *C* on *Pt*. *Pt* reaches a minimum value when *F* decreases and *C* increases. *Pt* reaches a maximum value when *F* increases and *C* decreases. **Figure 8c** demonstrates the effect of the interaction between *F* and *L* on *Pt*. Compared with *L*, the effect of *F* on *Pt* is obvious. When *F* is 0.004370 kg/s and *L* is 182 mm, *Pt* is the smallest. When *F* is 0.013110 kg/s and

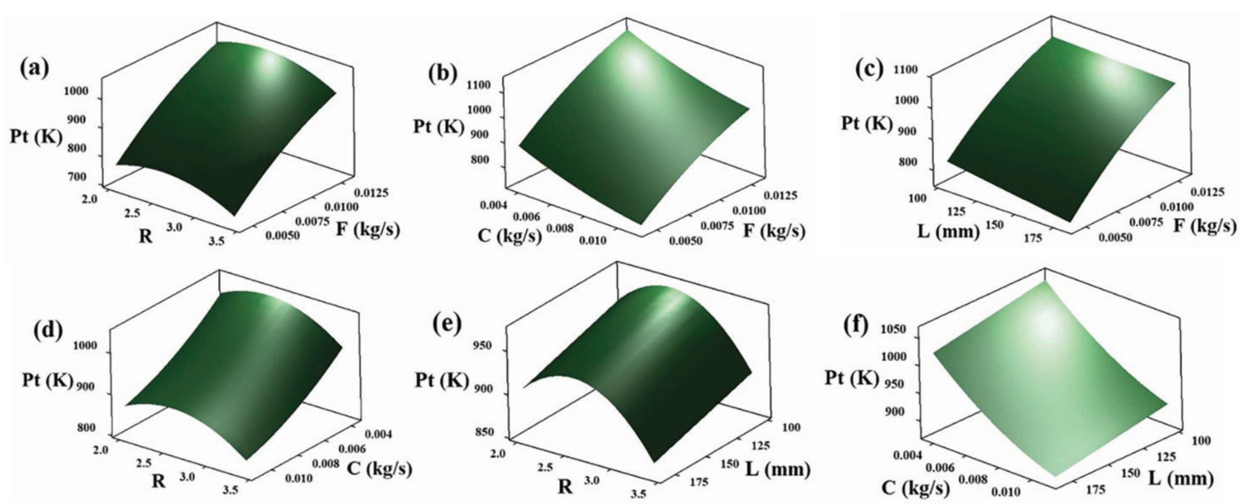

Figure 8: Response surface graphs for particle temperature: a) effect of F and R, b) effect of F and C, c) effect of F and L, d) effect of R and C, e) effect of R and L and f) effect of C and L

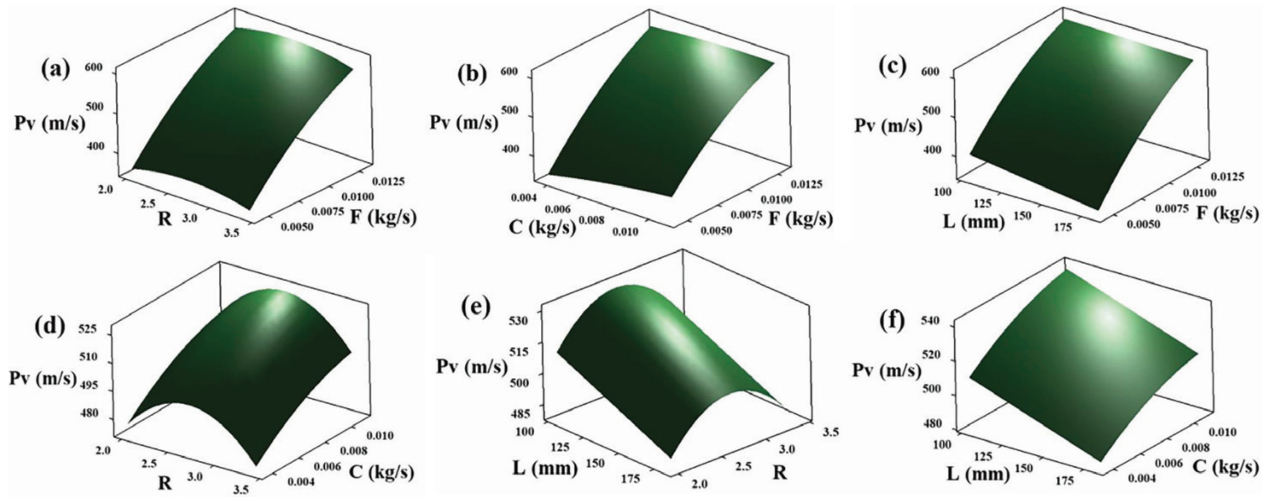

Figure 9: Response surface graphs for particle velocity: a) effect of F and R, b) effect of F and C, c) effect of F and L, d) effect of R and C, e) effect of R and L, and f) effect of C and L

L is 102 mm, *Pt* is the largest. The effect of the interaction between *R* and *C* on *Pt* is depicted in **Figure 8d**. When *R* increases and *C* decreases, *Pt* first increases and then decreases. *Pt* reaches a minimum value when *R* and *C* increase simultaneously. The influence of the interaction between *R* and *L* on *Pt* is presented in **Figure 8e**. When *R* and *L* increase at the same time, *Pt* first increases and then decreases. *Pt* is the smallest when *R* is 3.4 and *L* is 182 mm. The effect of the interaction between *C* and *L* on *Pt* is plotted in **Figure 8f**. The effect of *C* on *Pt* is the same as the effect of *L* on *Pt*. *Pt* reaches a minimum value when *C* and *L* increase simultaneously. *Pt* is the largest when *C* is 0.001471 kg/s and *L* is 102 mm.

Figure 9 exhibits the effects of factor interactions on particle velocity. The influence of the interaction between *F* and *R* on *Pv* is shown in **Figure 9a**. Compared with *F*, the effect of *R* on *Pv* can be ignored. *Pv* is always the maximum value when *F* is fixed and *R* is 2.7. The influence of the interaction between *F* and *C* on *Pv* is illustrated in **Figure 9b**. The effect of *F* on *Pv* is the same as the effect of *C* on *Pv*. When *F* and *C* increase together, *Pt* rises significantly. When *F* is 0.013110 kg/s and *C* is 0.013241 kg/s, *Pv* is the largest. **Figure 9c** demonstrates the effect of the interaction between *F* and *L* on *Pv*. Compared to *L*, the effect of *F* on *Pv* is obvious. *Pv* reaches a maximum value when *F* increases and *L* decreases. *Pv* is the smallest when *F* is 0.004370 kg/s and *L* is 182 mm. The influence of the interaction between *R* and *C* on *Pv* is shown in **Figure 9d**. When *R* and *C* increase at the same time, *Pv* first rises and then drops. *Pv* is the largest when *R* is 2.7 and *C* is 0.013241 kg/s. The influence of the interaction between *R* and *L* on *Pv* is presented in **Figure 9e**. When *R* and *L* increase concurrently, *Pv* first rises and then drops. *Pv* is the largest when *R* is 2.7 and *L* is 102 mm. **Figure 9f** shows the effect of the interaction between *C* and *L* on *Pv*. The effect of *C* on *Pv* is opposite to the effect of *L* on *Pv*. When *C* increases and *L* decreases, *Pv* increases significantly. *Pv* is the largest when *C* is 0.013241 kg/s and *L* is 102 mm.

3.2.3 Determination of OSP

To obtain Al-based fully AMCs with low porosity, it is necessary to make more sizes of Al-based amorphous alloy particles to reach a high velocity and semi-molten state before impacting the substrate. Due to the limited glass-forming ability of Al-based amorphous alloys, the particles with small to medium sizes are more easily able to form Al-based fully AMCs.[2] Therefore, the optimization goals of RSM in this study are maximization of particle velocity and more particles with small-to-medium sizes impacting the substrate in a semi-molten state.

According to the optimization strategy exhibited in Equations (14)–(17), the response surface equations for particle temperature (*Pt*) and particle velocity (*Pv*) were combined with the optimization goals to obtain the corresponding optimization results (**Figure 10**). Among them, the desirability of particle velocity and temperature is 0.93085 and 0.67486, respectively. The composite desirability is 0.7926 and close to 1, which indicates that the OSP predicted by RSM satisfies the optimization in-

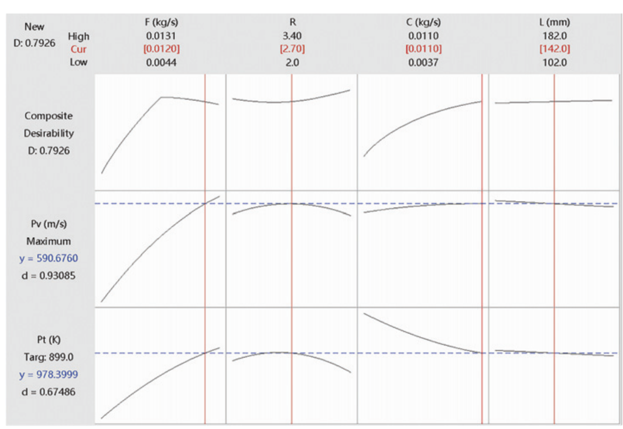

Figure 10: Optimization analysis results for OSP

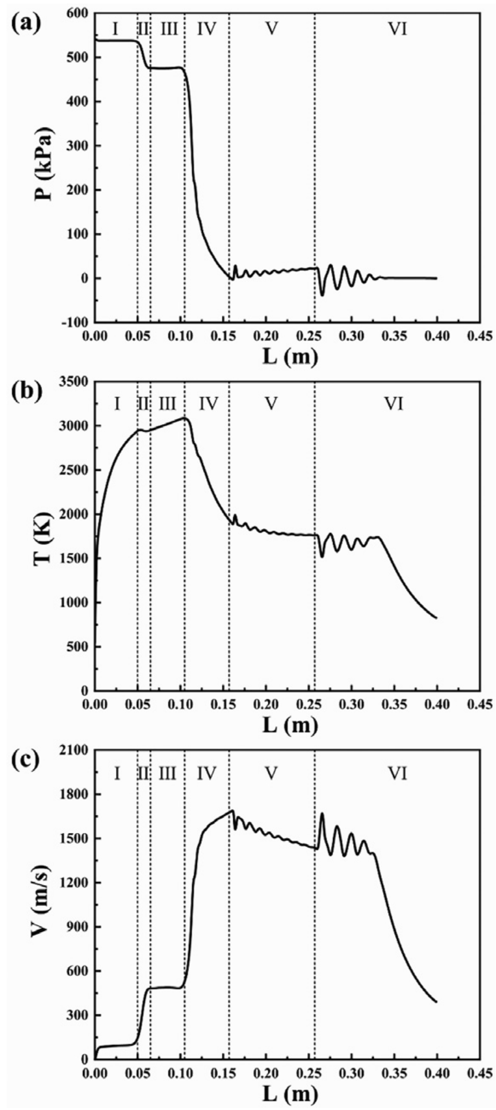

Figure 11: The a) pressure, b) temperature, and c) velocity of the flame flow based on OSP. (I), (II), (III), (IV), (V), and (VI) represent combustion chamber, convergent nozzle, mixing chamber, C-D nozzle, barrel, and free jet region, respectively

tent. Based on the OSP predicted by RSM (**Table 5**), the flame flow field (**Figure 11**) and the particle in-flight behavior (**Figure 12**) of the warm-spraying process were simulated using numerical simulation methods. In **Figure 11a**, the flame flow pressure in the combustion chamber has a maximum value and remains constant. It falls rapidly at the inlet of the C-D nozzle and eventually stabilizes at 0 kPa in the free jet region. In **Figure 11b**, the flame flow temperature reaches a peak of 3083 K at the end of the mixing chamber. When the flame flows into the C-D nozzle, the flame flow temperature begins to drop and eventually drops to 827 K. In **Figure 11c**, the velocity of flame flow reaches a peak of 1687 m/s at the barrel entrance. There are four complete Mach cones formed in the free jet region, which play a crucial role in the particle acceleration. In the corresponding flame flow field conditions, the 10–35 μm particles reach a semi-molten state before impacting the substrate (**Figure 12a**). The particles of almost all sizes maintain relatively stable and higher axial velocities before impacting the substrate (**Figure 12b**). Moreover, the simulation results show that the temperature and velocity of 30 μm particles when they hit the substrate are 977.069 K and 589.788 m/s, respectively. Compared with the temperature (978.3999 K) and velocity (590.676 m/s) of particles predicted by the RSM (**Figure 10**), the relative errors are respectively 0.15 % and 0.14 %, which further proves the validity of the optimal results predicted by RSM.

3.3 Experimental validation

Figure 13a shows the SEM images of Al-based amorphous alloy powders. The powders produced by gas atomization were mainly spherical or near-spherical particles. According to the OSP (**Table 5**), the Al-based AMCs were prepared using warm-spraying experiments. **Figure 13b** shows the XRD patterns of the $Al_{86}Ni_{6.75}Co_{2.25}Y_{3.25}La_{1.75}$ amorphous alloy powders and as-sprayed Al-based AMCs. The diffuse pattern and the

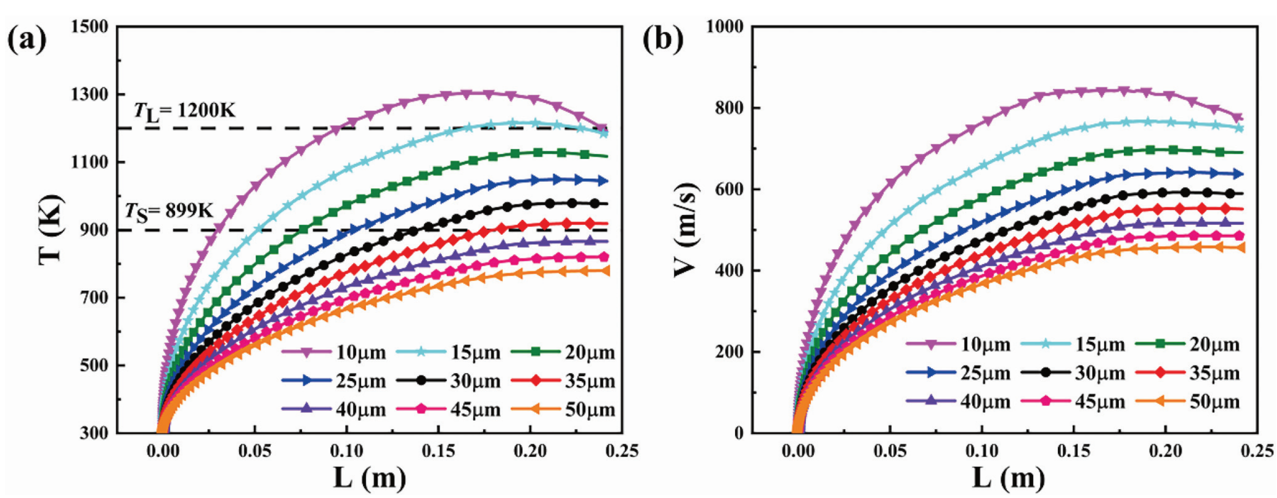

Figure 12: The a) temperature and b) velocity of particles based on OSP

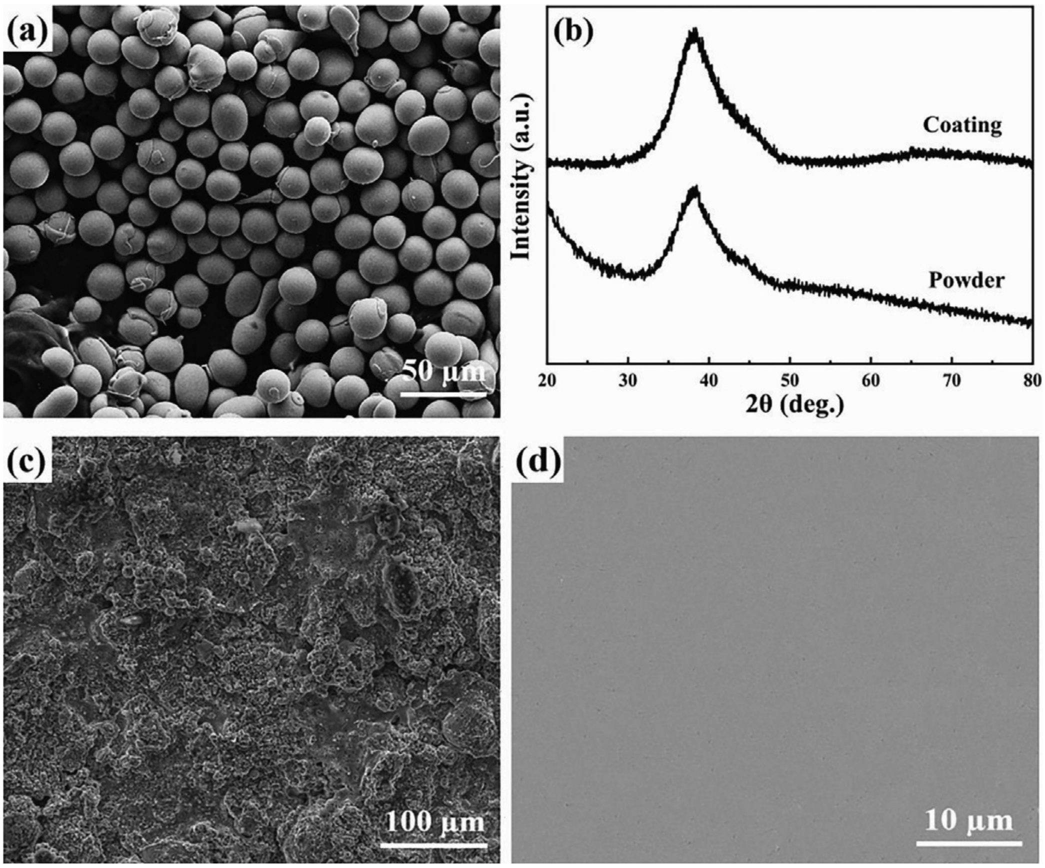

Figure 13: a) SEM image of the $Al_{86}Ni_{6.75}Co_{2.25}Y_{3.25}La_{1.75}$ amorphous alloy powders, b) XRD patterns of the $Al_{86}Ni_{6.75}Co_{2.25}Y_{3.25}La_{1.75}$ amorphous alloy powders and the as-sprayed Al-based AMCs, c) Surface morphology and d) cross-section structure of the as-sprayed Al-based AMCs

absence of any peaks associated with crystalline phases indicate that they are fully amorphous. **Figure 13c** and **13d** illustrate the surface morphology and cross-sectional structure of the as-sprayed Al-based AMCs. Al-based amorphous alloy powders are deposited on the substrate in a semi-molten state and the coating exhibits a uniform and dense structure with 0.08 % porosity. In summary, the Al-based fully AMCs with a porosity of 0.08 % were prepared using warm-spraying experiments based on the OSP predicted by RSM.

Table 5: OSP predicted by RSM for specific optimization intent

Spraying parameters	Value
Reactant flow rate (kg/s)	0.012047
O/F ratio	2.70
Coolant flow rate (kg/s)	0.011034
Spraying distance (mm)	142

4 CONCLUSIONS

In this paper, numerical simulations and RSM were combined to study the effect of the warm-spraying process parameters on the particle temperature and velocity and to predict the OSP. According to the OSP, the Al-based, fully AMCs with low porosity were prepared using warm-spraying experiments. The main conclusions were as follows:

(1) The influences of spraying parameters (reactant flow rate, O/F ratio, coolant flow rate, and spraying distance) on particle temperature and velocity were investigated by numerical simulation methods. The particle temperature and velocity increase with the reactant flow rate. The particles have the highest temperature and velocity at an O/F ratio of 2.7. Compared with the particle velocity, the particle temperature is significantly affected by the coolant flow rate and drops as the coolant flow rate rises. With the increase in spraying distance, the temperature and velocity of the particle gradually decrease. The 10–35 μm particles hit the substrate in a semi-molten state when the spraying distance is 142 mm.

(2) The RSM was used to investigate the influence of interactions between spraying parameters on particle temperature and velocity and to analyze their sensitivity. The reactant flow rate has the maximum effect on the particle temperature and velocity, followed by the coolant flow rate, O/F ratio, and spraying distance.

(3) The OSP predicted by the RSM were: 0.012047 kg/s for the reactant flow rate, 0.011034 kg/s for the coolant flow rate, 2.7 for the O/F ratio, and 142 mm for the spraying distance. According to the OSP, the warm-spraying process was simulated using numeri-

cal simulation methods to verify the viability of the RSM optimization process and to obtain the 10–35 μm size range of the sprayed particles. Finally, the Al-based fully AMCs with a porosity of 0.08% were prepared by warm-spraying experiments.

Acknowledgements

This work was supported by Natural Science Foundation of Liaoning Province under Grant No. 2022-MS-364; Fushun Revitalization Talents Program under Grant No. FSYC202107011. The financial support provided by the China Scholarship Council (CSC) is greatly acknowledged.

5 REFERENCES

[1] H. Guo, C. B. Jiang, B. J. Yang, J. Q. Wang, Deformation behavior of Al-rich metallic glasses under nanoindentation, J. Mater. Sci. Technol., 33 (**2017**), 1272–1277, doi:10.1016/j.jmst.2016.10.014

[2] N. C. Wu, L. Zuo, J. Q. Wang, E. Ma, Designing aluminum-rich bulk metallic glasses via electronic-structure-guided microalloying, Acta Mater., 108 (**2016**), 143–151, doi:10.1016/j.actamat.2016.02.012

[3] N. C. Wu, J. B. Lian, R. Wang, R. H. Li, W. Liu, Effect of element types on the glass forming ability of Al-TM-RE ternary metallic glasses using electron structure guiding, J. Alloys Compd., 723 (**2017**), 123–128, doi:10.1016/j.jallcom.2017.06.262

[4] M. H. Gao, S. D. Zhang, B. J. Yang, S. Qiu, H. W. Wang, J. Q. Wang, Prominent inhibition efficiency of sodium nitrate to corrosion of Al-based amorphous alloy, Appl. Surf. Sci., 530 (**2020**), 147211, doi:10.1016/j.apsusc.2020.147211

[5] L. M. Zhang, S. D. Zhang, A. L. Ma, H. X. Hu, Y. G. Zheng, B. J. Yang, J. Q. Wang, Influence of sealing treatment on the corrosion behavior of HVAF sprayed Al-based amorphous/nanocrystalline coating, Surf. Coat. Technol., 353 (**2018**), 263–273, doi:10.1016/j.surfcoat.2018.08.086

[6] L. M. Zhang, S. D. Zhang, A. L. Ma, H. X. Hu, Y. G. Zheng, B. J. Yang, J. Q. Wang, Thermally induced structure evolution on the corrosion behavior of Al-Ni-Y amorphous alloys, Corros. Sci., 144 (**2018**), 172–183, doi:10.1016/j.corsci.2018.08.046

[7] C. L. Tan, H. M. Zhu, T. C. Kuang, J. Shi, H. W. Liu, Z. W. Liu, Laser cladding Al-based amorphous-nanocrystalline composite coatings on AZ80 magnesium alloy under water cooling condition, J. Alloys Compd., 690 (**2017**), 108–115, doi:10.1016/j.jallcom.2016.08.082

[8] C. G. Pei, Z. X. Guo, J. G. Xiao, Effect of laser remelting treatment on $Al_{85}Ni_8Y_4Ce_3$ amorphous coating, Surf. Eng., 37 (**2021**), 642–649, doi:10.1080/02670844.2020.1800347

[9] J. Henao, A. Concustell, I. G. Cano, S. Dosta, N. Cinca, J. M. Guilemany, T. Suhonen, Novel Al-based metallic glass coatings by Cold Gas Spray, Mater. Des., 94 (**2016**), 253–261, doi:10.1016/j.matdes.2016.01.040

[10] C. C. Sun, X. L. Zhou, C. Xie, L. L. Xu, R. Z. Li, B. B. Liu, Formation of Al-based amorphous/nanocrystalline coatings by cold spraying, Surf. Coat. Technol., 389 (**2020**), 125644, doi:10.1016/j.surfcoat.2020.125644

[11] L. Jin, L. Zhang, K. G. Liu, Z. G. Che, K. Li, M. Zhang, B. Zhang, Preparation of Al-based amorphous coatings and their properties, J. R. Earths, 39 (**2021**), 340–347, doi:10.1016/j.jre.2020.04.018

[12] F. Presuel-Moreno, M. A. Jakab, N. Tailleart, M. Goldman, J. R. Scully, Corrosion-resistant metallic coatings, Mater. Today, 11 (**2008**), 14–23, doi:10.1016/S1369-7021(08)70203-7

[13] N. R. Tailleart, B. Gauthier, S. Eidelman, J. R. Scully, Metallurgical and physical factors controlling the multi-functional corrosion properties of pulsed thermal-sprayed Al-Co-Ce coatings, Corros. Sci., 68 (**2012**), 035006-1–035006-26, doi:10.5006/1.3693697

[14] J. B. Cheng, B. L. Wang, Q. Liu, X. B. Liang, In-situ synthesis of novel Al-Fe-Si metallic glass coating by arc spraying, J. Alloys Compd., 716 (**2017**), 88–95, doi:10.1016/j.jallcom.2017.05.032

[15] H. X. Chen, D. J. Kong, Effects of laser remelting speeds on microstructure, immersion corrosion, and electrochemical corrosion of arc–sprayed amorphous Al–Ti–Ni coatings, J. Alloys Compd., 771 (**2019**), 584–594, doi:10.1016/j.jallcom.2018.08.252

[16] J. B. Cheng, Y. Feng, C. Yan, X. L. Hu, R. F. Li, X. B. Liang, Development and characterization of Al-based amorphous coating, JOM, 72 (**2020**), 745–753, doi:10.1007/s11837-019-03966-y

[17] M. H. Gao, W. Y. Lu, B. J. Yang, S. D. Zhang, J. Q. Wang, High corrosion and wear resistance of Al-based amorphous metallic coating synthesized by HVAF spraying, J. Alloys Compd., 735 (**2018**), 1363–1373, doi:10.1016/j.jallcom.2017.11.274

[18] Z. D. Zhou, Z. B. Zhang, Y. X. Chen, X. B. Liang, B. L. Shen, Composition optimization of Al-Ni-Ti alloys based on glass-forming ability and preparation of amorphous coating with good wear resistance by plasma spray, Surf. Coat. Technol., 408 (**2021**), 126800, doi:10.1016/j.surfcoat.2020.126800

[19] H. Katanoda, T. Kiriaki, T. Tachibanaki, J. Kawakita, S. Kuroda, M. Fukuhara, Mathematical modeling and experimental validation of the warm spray (two-stage HVOF) Process, J. Therm. Spray Technol., 18 (**2009**), 401–410, doi:10.1007/s11666-009-9299-0

[20] S. Kuroda, M. Watanabe, K. H. Kim, H. Katanoda, Current Status and Future Prospects of Warm Spray Technology, J. Therm. Spray Technol., 20 (**2011**), 653–676, doi:10.1016/B978-0-85709-769-9.00007-5

[21] H. Jafari, S. Emami, Y. Mahmoudi, Numerical investigation of dual-stage high velocity oxy-fuel (HVOF) thermal spray process: A study on nozzle geometrical parameters, Appl. Therm. Eng., 111 (**2017**), 745–758, doi:10.1016/j.applthermaleng.2016.09.145

[22] C. Pierlot, L. Pawlowski, M. Bigan, P. Chagnon, Design of experiments in thermal spraying: A review, Surf. Coat. Technol., 202 (**2008**), 4483–4490, doi:10.1016/j.surfcoat.2008.04.031

[23] G. A. Clavijo-Mejía, D. G. Espinosa-Arbeláez, J. A. Hermann-Muñoz, A. L. Giraldo-Betancur, J. Muñoz-Saldaña, Effect of HVOF Process Parameters on TiO_2 Coatings: An Approach Using DoE and First-Order Process Maps, J. Therm. Spray Technol., 28 (**2019**), 1160–1172, doi:10.1007/s11666-019-00895-9

[24] W. Jibran, J. Hogan, A. McDonald, Towards optimization of thickness, hardness, and porosity of low-pressure cold sprayed WC-Ni coatings, Int. J. Adv. Manuf. Technol., 116 (**2021**), 2149–2160, doi:10.1007/s00170-021-07500-w

[25] S. Sauceda, S. Lascano, J. Núñez, C. Parra, C. Arévalo, L. Béjar, Effect of HVOF processing parameters on Cr_3C_2–NiCr hard coatings deposited on AISI 4140 steel, Eng. Sci. Technol., 39 (**2023**), 101342, doi:10.1016/j.jestch.2023.101342

[26] L. Qiao, Y. P. Wu, S. Hong, J. Cheng, Z. Wei, Influence of the high-velocity oxygen-fuel spray parameters on the porosity and corrosion resistance of iron-based amorphous coatings, Surf. Coat. Technol., 366 (**2019**), 296–302, doi:10.1016/j.surfcoat.2019.03.046

[27] N. Pulido-González, S. García-Rodríguez, M. Campo, J. Rams, B. Torres, Application of DOE and ANOVA in Optimization of HVOF Spraying Parameters in the Development of New Ti Coatings, J. Therm. Spray Technol., 29 (**2020**), 384–399, doi:10.1007/s11666-020-00989-9

[28] J. Cheng, Y. P. Wu, S. Hong, J. B. Cheng, L. Qiao, Y. J. Wang, S. S. Zhu, Spray parameters optimization, microstructure and corrosion behavior of high-velocity oxygen-fuel sprayed non-equiatomic CuAlNiTiSi medium-entropy alloy coatings, Intermetallics, 142 (**2022**), 107442, doi:10.1016/j.intermet.2021.107442

[29] S. J. S. Chelladurai, K. Murugan, A. P. Ray, M. Upadhyaya, V. Narasimharaj, S. Gnanasekaran, Optimization of process parameters using response surface methodology: A review, Mater. Today: Proc., 37 (**2021**), 1301–1304, doi:10.1016/j.matpr.2020.06.466

[30] B. Y. Han, J. J. Chu, W. B. Du, K. B. Zhou, M. Q. Cong, F. F. Cui, W. X. Hang, S. Zhu, Optimization of Ni60A Coating Quality by Supersonic Plasma Spraying Based on Response Surface Methodology, J. Therm. Spray Technol., 32 (**2023**), 1596–1610, doi:10.1007/s11666-023-01580-8

[31] K. Palanisamy, S. Gangolu, J. M. Antony, Effects of HVOF spray parameters on porosity and hardness of 316L SS coated Mg AZ80 alloy, Surf. Coat. Technol., 448 (**2022**), 128898, doi:10.1016/j.surfcoat.2022.128898

[32] X. Gao, C. Li, D. C. Zhang, H. X. Gao, X. Han, Numerical analysis of the activated combustion high-velocity air-fuel (AC-HVAF) thermal spray process: A survey on the parameters of operation and nozzle geometry, Surf. Coat. Technol., 405 (**2021**), 126588, doi:10.1016/j.surfcoat.2020.126588

[33] J. Z. Ren, G. F. Zhang, Y. M. Rong, Y. S. Ma, A feature-based model for optimizing HVOF process by combining numerical simulation with experimental verification, J. Manuf. Process., 64 (**2021**), 224–238, doi:10.1016/j.jmapro.2021.01.017

[34] X. Y. Zhao, C. Li, S. Y. Li, H. S. Jiang, X. Han, Time-varying evolutionary mechanism analysis of the multiphase flow during high-velocity oxygen-fuel (HVOF) thermal spraying WC-12Co particle, Surf. Coat. Technol., 461 (**2023**), 129435, doi:10.1016/j.surfcoat.2023.129435

[35] X. X. Chen, C. Li, S. Y. Li, X. Han, H. S. Jiang, X. Y. Zhao, HVOF Spray Performance Optimization Analysis and Experimental Research of WC–12Co Coating on Ti Alloy, Met. Mater. Int., 29 (**2023**), 3548–3565, doi:10.1007/s12540-023-01458-y

[36] C. Li, X. Gao, Y. P. Yang, X. X. Chen, X. Han, Sensitivity Analysis of Process Parameters of Warm Spraying Process Based on Response Surface Method, J. Therm. Spray Technol., 31 (**2022**), 585–597, doi:10.1007/s11666-022-01319-x

[37] M. M. Liu, Z. X. Yu, Y. C. Zhang, H. J. Wu, H. L. Liao, S. H. Deng, Prediction and analysis of high velocity oxy fuel (HVOF) sprayed coating using artificial neural network, Surf. Coat. Technol., 378 (**2019**), 124988, doi:10.1016/j.surfcoat.2019.124988

[38] M. M. Liu, Research and implementation of artificial neural networks models for high velocity oxygen fuel thermal spraying, Université Bourgogne Franche-Comté, (2020)

[39] K. Malamousi, K. Delibasis, B. Allcock, S. Kamnis, Digital transformation of thermal and cold spray processes with emphasis on machine learning, Surf. Coat. Technol., 433 (**2022**), 128138, doi:10.1016/j.surfcoat.2022.128138

[40] U. M. R. Paturi, D. G. Vanga, S. Cheruku, S. T. Palakurthy, N. K. Jha, Estimation of abrasive wear of nanostructured WC-10Co-4Cr TIG weld cladding using neural network and fuzzy logic approach, Mater. Today: Proc., 78 (**2023**), 449–457, doi:10.1016/j.matpr.2022.10.266

[41] J. X. Yu, X. Liu, Y. Yu, Z. M. Li, S. B. Xu, H. D. Li, P. F. Liu, L. M. Wang, Effect of HVOF Spraying Process on Particle Behavior of Fe-Based Amorphous Alloy Coatings, J. Therm. Spray Technol., 31 (**2022**), 2448–2462, doi:10.1007/s11666-022-01476-z